Coastal tidal effects on industrial thermal plumes in satellite imagery

remote sensing

MDPI

Letter

Coastal Tidal Effects on Industrial Thermal Plumes in Satellite Imagery

Agnieszka Faulkner [1,*], Claire E. Bulgin [1,2] and Christopher J. Merchant [1,2]

[1] Department of Meteorology, University of Reading, Reading RG6 6BG, UK; c.e.bulgin@reading.ac.uk (C.E.B.); c.j.merchant@reading.ac.uk (C.J.M.)
[2] National Centre for Earth Observation, University of Leicester, Leicester LE1 7RH, UK
* Correspondence: agnieszka.walenkiewicz@pgr.reading.ac.uk

Received: 29 July 2019; Accepted: 6 September 2019; Published: 13 September 2019

Abstract: Coastal tidal effects on thermal plumes are investigated, exploiting remote sensing of two major coastal industrial installations. The installations use sea water as a coolant, which is then released back into coastal environments at a higher-than-ambient temperature, allowing the plume to be delineated from the ambient waters. Satellite-based thermal sensors observing the Earth at spatial resolutions of 90 and 100 m are used. It is possible to identify coastal features and thermal spatial distributions. This paper presents coastal tidal effects on detected plumes for two case studies: an intertidal embayment and open water exposure, both on the coast of the UK. We correlated the behaviours of thermal plumes using remotely sensed high resolution thermal imagery with tidal phases derived from tide gauges. The results show very distinct behaviours for the flood and ebb tides. The detected surface plume location was dependent on flow switching direction for the different types of tide. The detected surface area was dependent on the strength of the currents, with the largest area observed during the strongest currents. Understanding the dispersion of the plume is essential to influence understanding of any potential ecological impacts.

Keywords: industrial plumes; remote sensing; Landsat 8; ASTER; SST

1. Introduction

Coastal zones are sensitive ecosystems providing valuable habitats for varied flora and fauna, as well as economic benefits including tourism and leisure. Coastal areas are constantly changing because of interactions with weather and coastal waters, climate change effects, sea-level changes, land-use impacts and human-made infrastructures [1,2]. Tourism, maritime traffic, fishing, human-made coastal installations, etc. act as anthropogenic stressors on the coastal environment and may affect the distribution of marine species. Impacts vary spatially and temporally [3]. Therefore, it is important to monitor those zones, providing a basis for resolving stresses in space and time [3] and supporting sustainable coastal zone management [1].

Coastal regions remain challenging areas for Earth observation due to dynamic land–water boundaries and enhanced variability in shallow water regions. Field campaigns often do not get very close to the coast, limiting the investigated areas to regions offshore deep enough for the survey vessels. Tide observations from routine monitoring, coming from an extensive national network, are limited to point measurements. Numerous studies have used different modelling techniques in order to understand coastal dynamics [4–8]. In addition to the models, the use of high-resolution remote sensing data can contribute to better understanding of the coastal zone [9–12]. Despite the temporal trade-off associated with the satellite repeat-time coverage, remote sensing information has the advantage of high spatial resolution observations.

In this paper, satellite imagery is used to look at the coastal tidal effects on industrial thermal plumes. We use Landsat 8 and Advanced Spaceborne Thermal Emission and Reflection Radiometer (ASTER) products with the focus on the British coastal areas, in the vicinity of power stations using sea waters for cooling purposes. The outflow coolant water has temperature higher than ambient waters, enabling us to investigate coastal zones and gain understanding of surface water behaviour. We will refer to this coolant water outflow as a thermal plume throughout the remainder of this paper.

Previous studies have focused on understanding the nature of thermal plumes by integrating in situ measurements with thermal imagery from satellites [13] and portable thermal cameras [14], using high-resolution imagery to study SST distribution around power stations [15–18], investigating consistency between different sensors in thermal plume detection [19]. The spatial extent of the surface thermal plume was identified by comparison with observations taken during the same months prior to the power station operation, focusing on three locations: the bay [15,16], the harbour [15] and the open water [15]. For all regimes, the areas of the most significant temperature rise were limited close to the power stations and dissipated along the coast.

Thermal plumes have been used to study coastal dynamics in Daya Bay, on the coast of South China Sea. During the winter months, the plume is limited to small area westward of the power station, whereas in summer months plume area reaches 40–100 km^2 to the south-eastward of the bay [17]. The distinct seasonality of the thermal plume was attributed to strong mixing of the water column during the winter months, dispersing the warm water throughout the water column. During the summer months, with stratified waters, the less saline waters disperse close to the surface. Sudden drops in temperature in the thermal plume region have been attributed to strong mixing of the plume with ambient waters [14].

Ahn et al. (2006) [18] investigated thermal plumes in Younggwang coastal areas, Korea. They found that the occurrence of strong coastal currents and winds during winter and summer monsoons often results in a high rate of thermal dispersion in the southern and northern parts of the Younggwang coast. The work by the authors of [20] draws similar conclusions to his field campaign with CTD probes in the Bay of Bengal, attributing the plume direction and distribution to the prevailing currents.

For the two power stations located on the northern coast of Taiwan, the plume area and temperature difference was related to tidal regimes [13]. In both cases, the highest temperature rises covered a bigger area during flood tides than during ebb tides, although the overall plume area was larger during ebb tides. This suggested quicker spreading of the thermal plume during ebb tides as well as advection offshore.

Research into thermal plumes in Europe has focused on thermal pollution of rivers and river estuaries [21], making the coastal regions a good opportunity for further investigation. Major power generation facilities around the coast of Great Britain provide a range of case studies, including bays, channels and open water. We focus in this study on two installations: Heysham, located on the western coast of the UK in the Morecambe Bay adjacent to the extensive geological area of Heysham sands (Figure 1), and Sizewell, located on the eastern coast in Suffolk and discharging waters to the North Sea (Figure 2).

The purpose of this paper is to use remote sensing imagery to investigate tidal effects on industrial plumes. Both coastal bathymetry and tides influence the dispersion of thermal plumes from industry. This paper focuses on the extent to which remote sensing imagery can reveal the impact of tides on thermal plume dispersion. We use Landsat 8 and ASTER imagery of two regions near two industrial power stations. We detect thermal plumes in the region of interest (ROI) using a combination of water detection, mask expansion and thresholding techniques. We relate the detected plumes to calculated phase of tide based on the National Tide Gauge Network (NTNG) measurements. Finally, we create conditional probability maps of detected plumes occurrence. These results provide new spatial understanding for tidal effects along the British coast. This paper proceeds as follows. Section 2 describes the methodology, Section 3 presents the results, Section 4 provides the discussion of the results, and Section 5 summaries our findings.

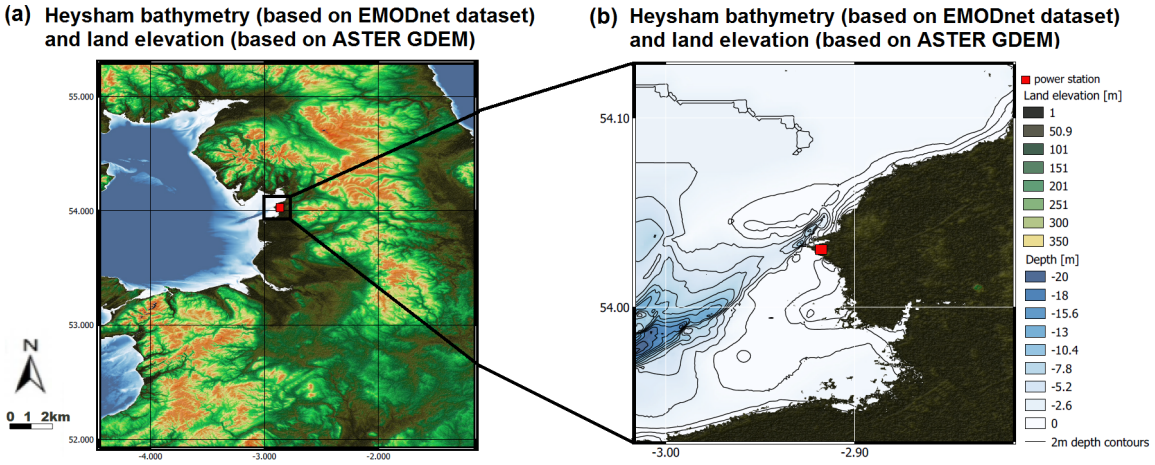

Figure 1. (**a**) Location of the Morecambe Bay, with Heysham power plant marked as a red square, with land elevation obtained from ASTER Global Digital Elevation Model (GDEM) and bathymetry obtained from European Marine Observation and Data Network (EMODnet) datasets. (**b**) Close-up of the region of interest (ROI), with detailed bathymetry with contours at 2 m depth intervals obtained from EMODnet dataset. Lighter colours represent shallower waters and darker colours deeper waters.

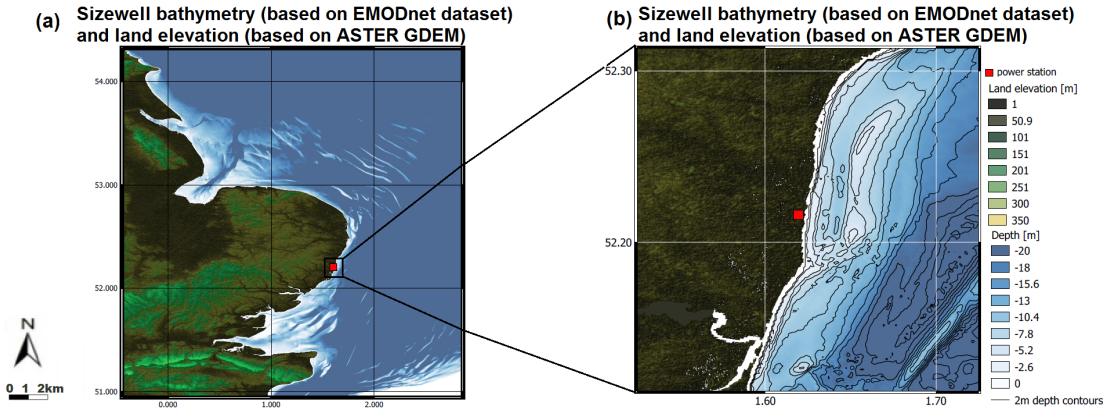

Figure 2. (**a**) Location of East Anglia, with Sizewell power plant marked as a red square, with land elevation obtained from ASTER GDEM and bathymetry obtained from EMODnet datasets. (**b**) Close-up of the ROI, with detailed bathymetry with contours at 2 m depth intervals obtained from EMODnet dataset. Lighter colours represent shallower waters and darker colours deeper waters.

2. Methods

We use high-resolution infrared and visible observations from the Operational Land Imager (OLI) and the Thermal Infrared Sensor (TIRS) on-board Landsat 8 and from ASTER on-board Terra. Landsat 8 is a satellite launched by the National Aeronautics and Space Administration (NASA) in collaboration with the United States Geological Survey (USGS). It has been operational since 11 February 2013. It has a return time of 16 days, providing high-resolution data over land and ocean across a swath of 185 km. The two push-broom instruments on-board, OLI and TIRS, cover visible, near-infrared (near-IR), short wave infrared (SWIR) and thermal infrared (TIR) wavelengths of the electromagnetic spectrum. Visible, near-IR and SWIR bands measure at 30 m resolution. The TIR wavelengths have resolution of 100 m, which is resampled using cubic convolution onto the 30 m grid prior to dissemination. Cloud cover information is provided, used here to identify clear-sky observations required for the purpose of the study.

ASTER is an instrument on-board the Terra satellite that has been in operation since December 1999 in a joint operational mission between NASA and Japan's Ministry of Economy, Trade and

Industry (METI). ASTER has three instruments: visible and near-infrared (VNIR), SWIR and TIR measuring at 15, 30 and 90 m resolution, respectively. With the same revisit time as Landsat 8, ASTER coverage is not as complete as it acquires data on a tasked basis. Typically we find most acquisitions of ASTER data in locations of interest are at night.

We extract satellite data centred on the power station location over a ROI with a spatial extent of 0.2° × 0.2°. The data are regridded from their 30 m raster resolution onto a fixed degree grid at 0.0005° in order to obtain all ASTER, OLI and TIRS data on a common grid while minimising sampling issues. TIR bands for ASTER come at the resolution of 90 m and are resampled using nearest neighbour methods, with gaps filled by linear 2D interpolation, onto our grid. A grid resolution of ~50 m is adequate to investigate coastal features and distinguish between land, beach, cloud and water regions.

Coastal regions are typically characterised by variable land–water boundaries and, in some cases, the presence of intertidal flats, requiring correct identification of the water line for each image. The water line is the boundary between the sea and a nonwater object (land, beach, mud flats, etc.). For daytime images we detect water using the Modified Normalised Difference Water Index (MNDWI) (Equation (1)) [22], an extension of the Normalised Difference Water Index (NDWI) [23] shown to perform better in coastal regions [24,25] and mixed pixels [22]. Since the MNDWI uses visible and SWIR bands in the equation, it is impossible to apply the same algorithm for the scenes retrieved at night. Therefore, to mask out land pixels in the night-time scenes, we used a statistical land mask derived from a set of daytime MNDWI imagery. Night-time imagery, with applied expanded statistical land mask derived from daytime images, has undergone thresholding to remove cold clouds and beaches. We apply a threshold of 276 K to band 13 of ASTER's data (10.2–10.9 μm), classifying every pixel with value below 276 K as contaminated by cold clouds or beach, and everything above that threshold as water. This enables masking of cold clouds, but does not fully mask the exposed beach regions. However, this has not been an issue in plume detection since the thermal features of the industrial plume are of higher temperature than the beaches. As night-time scenes are limited, the cloud detection could be verified visually to ensure that no obvious warm cloud features were evident in the region of the plume.

$$MNDWI = \frac{Green - SWIR}{Green + SWIR} \quad (1)$$

We retrieve sea surface temperature (SST) using optimal estimation [26]. Optimal estimation (OE) is an inverse method to estimate the state variables, given an initial estimate and simulations of the observations. The state variables retrieved are SST and atmospheric humidity. The simulations are run for a prior state obtained from numerical weather prediction (NWP) atmospheric profiles. The prior SST is daily gridded global sea surface temperature (level 4 SST) data from the European Space Agency Climate Change Initiative (ESA CCI) programme [27]. For each state vector there exists an "ideal, synthetic measurement" vector, and OE requires simulation of measurements as part of the retrieval process. Clear-sky observations are simulated using RTTOV [28,29] and ERA Interim profiles to represent the atmospheric state at the time of observation [30]. Given the actual measurements, the simulations and the prior state, OE returns the most probable state variables vector. CCI level 4 SST is not adapted to the feature resolution required for coastal zones, but rather reflects temperatures ~20 km offshore [31]. Since there is only one prior SST value per acquired satellite scene, it does not include the temperature variations across the scene, including those caused by the thermal plume. We therefore assign the uncertainty in our prior SST to be the biggest temperature difference across the scene (i.e., biggest difference between the plume and ambient waters in each scene) and after investigation this is set to 8 K.

Having retrieved SST for the coastal regions, all masked land and beach regions in the image are expanded using morphological dilation [32] to exclude warm shallow coastal waters that could mistakenly be interpreted as thermal plumes. Next, possible plumes are detected through identifying contiguous areas that pass given thermal thresholds of 1.5 K warmer than a chosen box of ambient

temperature of surface waters. The box of ambient waters is chosen for each image as a square area 5 km by 5 km of coastal waters at least 5 km offshore and not contaminated by the thermal plume or warm shallow waters. By examining the satellite imagery in which the plume region is evident, we found a consistent offshore region, common across all scenes that was outside of the plume extent. We calculate the average temperature in that box for each scene and treat it as surface ambient temperature for the whole image. The plume detection then compares the temperature of every water pixel to the ambient temperature. If the pixel was >1.5 K warmer than the ambient temperature, it was classified as a potential plume. The thermal threshold of 1.5 K was chosen after considering the uncertainty associated with the instruments and SST retrieval method. The TIRS instrument onboard Landsat 8 had radiometric errors of −2.1 K and −4.4 K at 300 K for Band 10 (10.6–11.2 µm) and Band 11 (11.5–12.5 µm), respectively, and high error variability, due to stray light artefacts after launch. In 2017, a new calibration process has reduced the residual variability to 0.51 K at 300 K for Band 10 and 0.84 K at 300 K for Band 11 [33]. The TIR subsystem for ASTER instrument has the signal-to-noise temperature difference of 0.3 K at 300 K. The radiometric accuracy of the retrieval varies between 1–3 K depending on the BT range [34]. Moreover, during summer and early autumn months, very shallow waters close to the coast can warm significantly during the day and applying a lower thermal threshold could mistakenly include those waters in the plume analysis, obscuring the results.

From the pixels identified as warmer than ambient we then use our algorithm to detect the plume itself. Small clusters of warm pixels (not more than two) that pass the threshold are masked out as noise. From the remaining aggregates of warm water pixels, the detected plume is identified as the object nearest to the power station, discarding other aggregates and treating them as ambient waters.

For each observation, we identify the phase of the tide at the ROI. Tide measurements used in this study come from the National Tide Gauge Network (NTNG). The NTNG provides extensive monitoring of the tides in 44 point locations around the UK coast. We relate the satellite imagery to the tidal measurements to provide new insight into flow dynamics around the British coast. Figure 3 presents the data used and methods applied throughout the analysis process.

Since tidal measurements resemble a continuous periodic function, with measurements every 15 min, tidal data for the period of 3 to 7 days (including the date of the satellite overpass as the central day) has been fitted to a sine function (Equation (2)), where $H(t)$ is the height of water at satellite overpass time, $\bar{H}$ is average height of water, A is the water height amplitude, f is frequency, t is time and ϕ is the phase offset.

All the observations have been sorted based on the phase of the tide, θ (Equation (3)). Values of θ range from 0 to 360°, where 0–90 and 270–360° are periods of rising water levels and 90–270 ° is the period of receding water.

$$H(t) = \bar{H} + Asin(2\pi ft + \phi) \quad (2)$$

$$\theta = 2\pi ft + \phi \quad (3)$$

After sorting the satellite observations and detected plumes based on the phase of tide, we create probability density maps. The method used is a follows. We first apply the plume detection to every image. We then sum all plumes detected in images for specific phase of tide (i.e., all plumes detected in flood tide imagery and all plumes detected in ebb tide imagery) for a given location and divide by the total number of observation during the specific phase of tide (i.e., all images during flood tide or during ebb tide) used for the site, presenting the data as probabilities.

To distinguish between ebb and flood currents, we use Norwegian Meteorological Institute (MET Norway) operational ocean model data. The Norwegian MET operational ocean model covers the area of −28.556 to 79.801°E and 46.563 to 87.686°N with a grid spacing of 4 km. The model uses the atmospheric forcing from European Centre for Medium-Range Weather Forecasts (ECMWF) 0.125°, tides from a series of fully-global models of ocean tides, and vertical boundary conditions from Arctic 20 km. There are two model runs a day and the hourly forecasts can be provided up to 5 days in advance. The ebb (flood) tides are in a southerly (northerly) direction for Sizewell and north-easterly

(south-westerly) for Heysham. The strengths of currents vary, with weaker currents being observed during the beginning and end of each tide phase and the strongest currents being observed around the middle of the tide phase. We have superimposed the example direction of the sea currents from the MET Norway data associated with the tide phase on our probability maps.

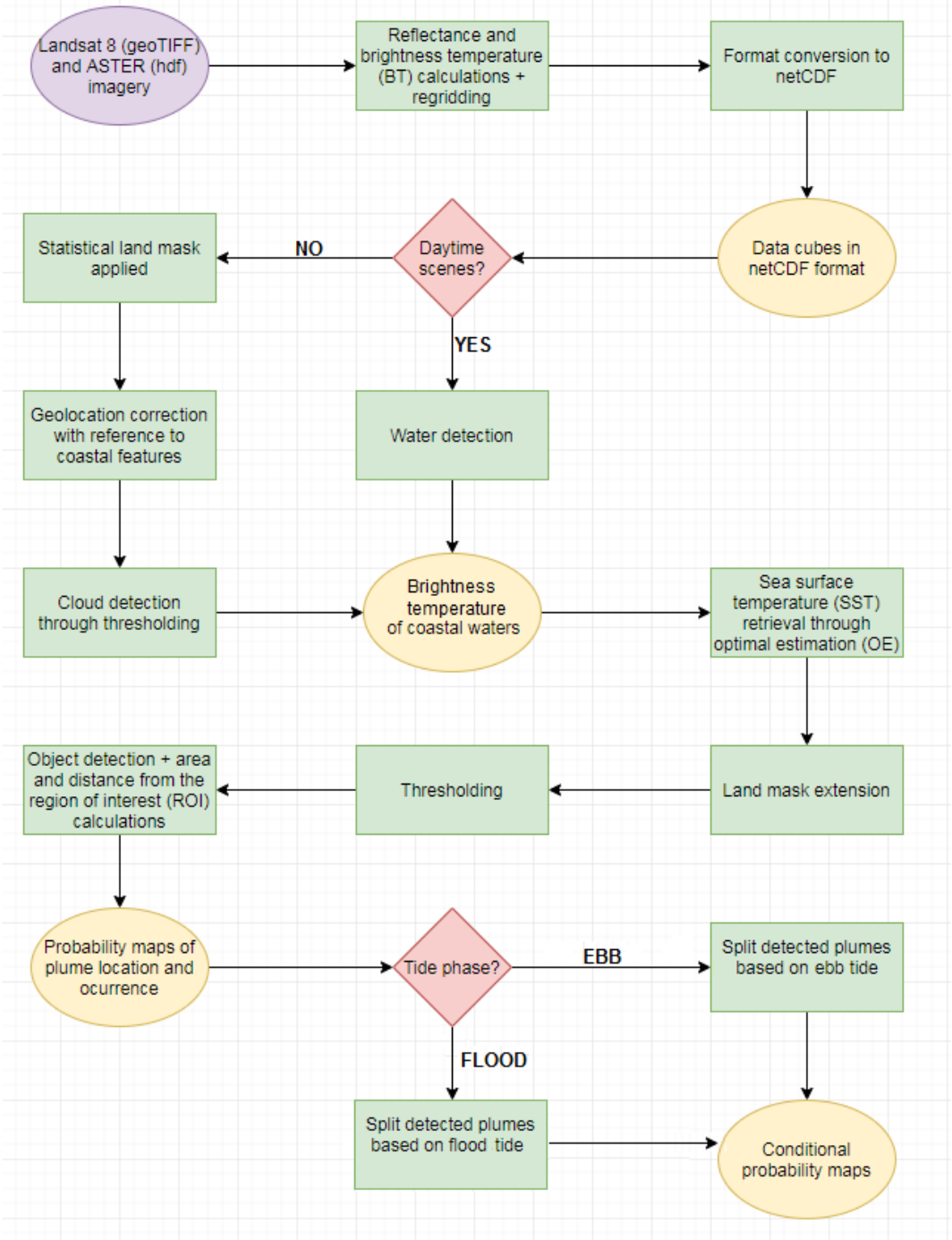

Figure 3. Workflow plan. Data used are presented in the oval shapes. Yellow ovals represent generated products and purple ovals represent existing datasets. Methods applied are presented as green rectangles and decisions as red diamonds. netCDF data format mention in the plan is the Network Common Data Form.

3. Results

3.1. Heysham as Example of Intertidal Embayment

Morecambe Bay is the largest macro-tidal embayment in north-west England with very dynamic intertidal area [35]. Our ROI is centred next to Heysham Sands and surrounded by tidal flats formed by mud or wet sand deposited by tides. The durations of the tides are unequal with the ebb tide lasting longer than the flood tide by ~40 min [36]. Heysham water height, measured at the tide gauge point, ranges between just 1 and 3 m during ebb tide and between 7 and 10 m during flood tide. The location as well as the extent of the thermal plume are highly dependent on the phase of the tide.

During the ebb tide, the regions of Heysham Sands near the ROI are exposed (Figure 4b). The plume is easy to detect (Figure 4a), starting at the end of the two pipelines coming out of the power station and moving with the currents associated with the ebb tide (Figure 4b). Other warm water puddles are localised very close to the exposed sand bank areas and do not extend. The plume stretches in the direction of the open ocean, exiting the Morecambe bay (Figure 4a) along the deep water channel stretching south-westward. This can be seen in the bathymetry maps (Figure 4a). The detected plume covers a narrow, elongated region. In most cases, the plume's length does not exceed 5 km and is confined to a narrow belt. However, on a few occasions, the plume's length reaches over 7 km extending further towards the deep water channel (Figure 4a). Such behaviour was noticed during the middle phase of the ebb tide, when the currents were the strongest.

During the flood tide, the intertidal flats are hidden with waters rising, and the thermal plume is trapped close to the coastline (Figure 4c), which is associated with the direction of the currents during the flood tide (Figure 4d). There are two scenarios where currents cause the plume to spread south east towards the river estuary or northwards and recirculate into the Heysham Harbour. When the thermal plume is advected towards Heysham Harbour, the flood tide is in the beginning or middle phase. In the first case, following the lowest water level, when the sand banks were still exposed and the currents have just changed the direction, flowing north-eastwards. This causes the plume to move northwards of the outlet pipes along the still exposed sand banks. During mid-flood, the sand banks are beginning to be covered with sea water and the north-eastwards currents are picking up, flowing into the bay. Strong currents cause the plume to move north-eastwards into the bay. In later phases of the flood tide, with currents decreasing in strength and no exposed sandbanks, the plume is located south and south-east off the discharge pipes close to the coastline. In most cases (18 out of 23 images), the detected plume seems to be restricted to an area between the coast and 3.5–4 km offshore, suggesting good mixing of the waters. Mixing would cause further dispersion of the actual plume, however, as the detected plume needs to fulfill the criterion of 1.5 K above ambient temperature, a restricted area is indicative of a good mixing.

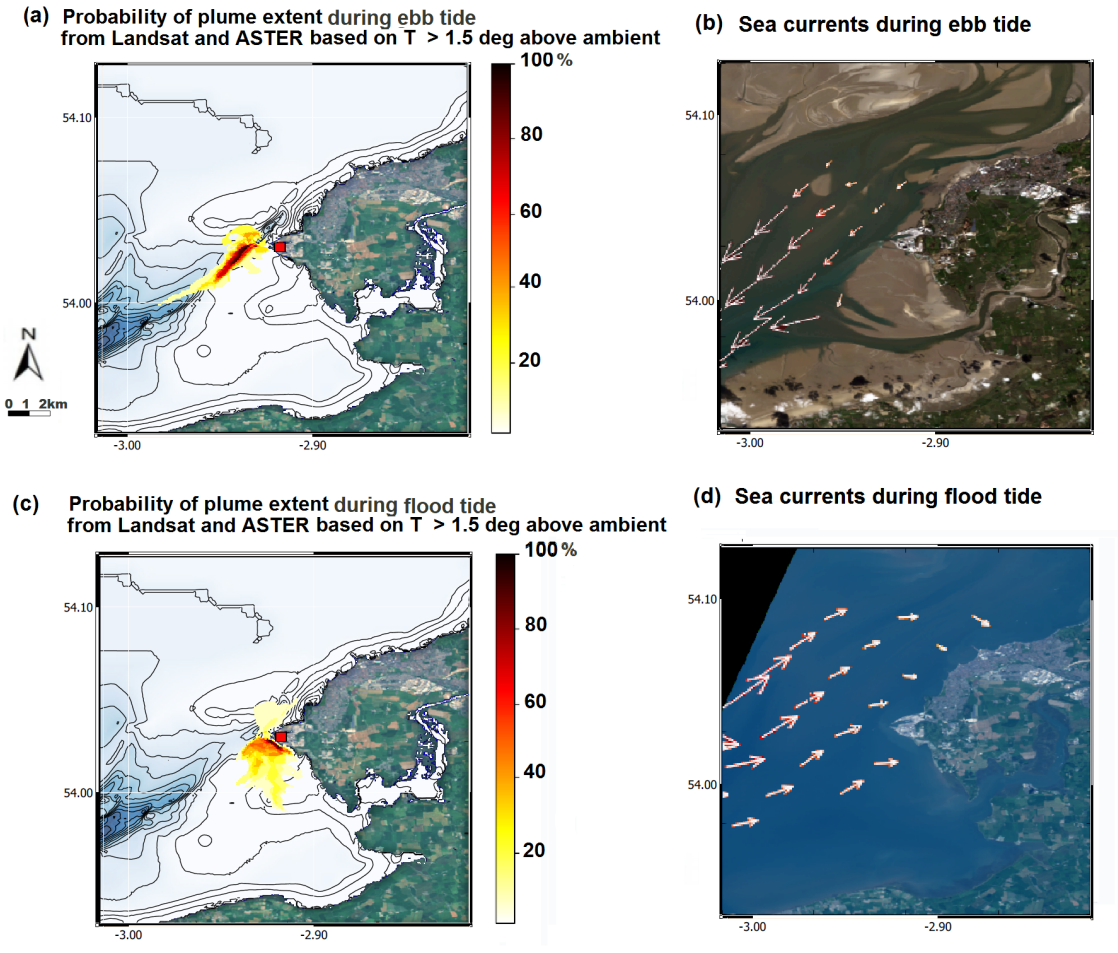

Figure 4. (**a**) Probability density map of thermal plume location and reach during ebb tide with darker colours presenting higher probability and lighter colours lower probability. On some occasions, the sands are exposed (see b), whereas, on other occasions, the sands are not exposed to the same extent. The plume follows the same direction, along the deeper water channel, independent of the amount of sands exposed. (**b**) Corresponding RGB composite of an example daytime scene during ebb tide with waters visible in dark-blue–green, exposed sands visible in light-brown, land in dark-green and harbour and built-up areas in white. The arrows represent the currents visualised by MET Norway. During the ebb tide, weaker flow is represented by smaller arrows and stronger flow is represented by bigger arrows. (**c**) Probability density map of thermal plume location of reach during flood tide, with darker colours presenting higher probability and lighter colours lower probability. (**d**) Corresponding RGB composite depicting example daytime scene during flood tide with waters visible as dark-blue, land in dark-green and harbour and built-up areas in white. The arrows, visualised by MET Norway, represent the direction of flow during flood tide with weaker flow being represented by smaller arrows and stronger flow being represented by bigger arrows.

3.2. Sizewell as Example of Open Water Exposure

The Suffolk coast is an example of open water exposure with Sizewell–Dunwich Banks located offshore, parallel to the coast, close to the ROI. These naturally-occurring structures are relatively narrow (~2 km in width) underwater sand banks, over 10 km in length [37] and were created by wave energy, currents and sediment transport, and they reduce wave energy. A few studies have shown that the growth of the banks (especially the Dunwich bank) has altered the direction and the height of approaching waves. The 20-year data record of annual average wind data indicates that the

predominant winds are south-westerly with transport directed towards the north-east [38]. There are no sand or mud banks large enough to be captured by the satellite imagery, as they exposed during different tidal phases. However, Sizewell is located ~100 km away from the amphidromic point in the southern part of the North Sea [39], which is a point where the tidal constituent amplitude is zero. This influences the pattern of tidal currents, which consists of flow nearly parallel to the coast (Figure 5b,d) reflected by the thermal plume forming an elongated area of warm water parallel to the coastline alternately north-east and south-west directions (Figure 5a,c). The location of the detected plume is highly dependent on the phase of the tide.

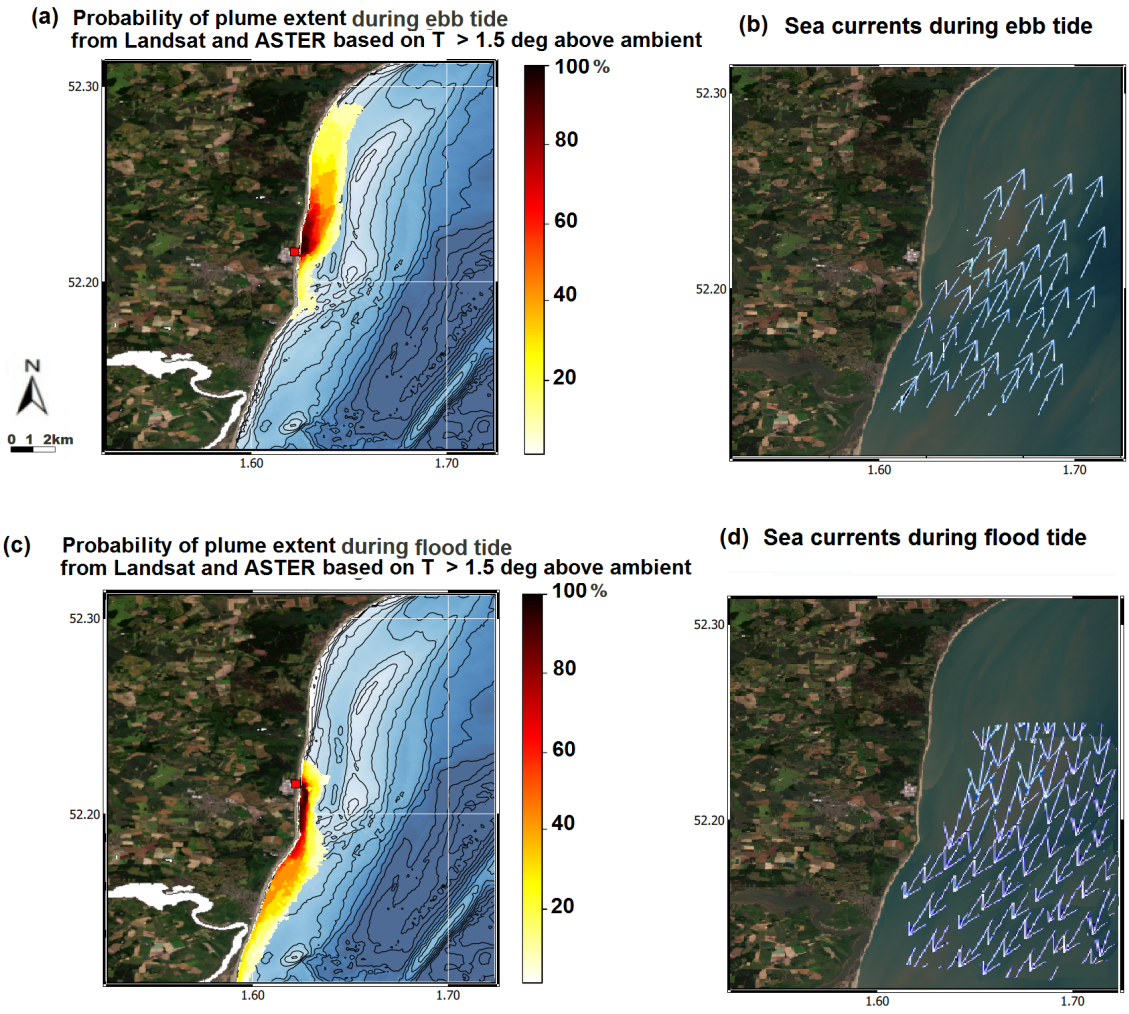

Figure 5. (**a**) Probability density map of thermal plume location and reach during ebb tide with darker colours presenting higher probability and lighter colours lower probability. (**b**) Corresponding RGB composite of an example daytime scene during ebb tide with waters visible in dark-blue–green, exposed sands visible in light-brown, land in dark green and harbour and built-up areas in white. The arrows represent the currents visualised by MET Norway. During the ebb tide, weaker flow is represented by smaller arrows and stronger flow is represented by bigger arrows. (**c**) Probability density map of thermal plume location of reach during flood tide with darker colours presenting higher probability and lighter colours lower probability. (**d**) Corresponding RGB composite depicting example daytime scene during flood tide with waters visible as dark-blue, land in dark-green and harbour and built-up areas in white. The arrows, visualised by MET Norway, represent the direction of flow during flood tide with weaker flow being represented by smaller arrows and stronger flow is represented by bigger arrows.

During the ebb tide, the tidal streams run northwards, which can be observed by the direction of the plume dispersion (Figure 5a). This flow direction is consistent throughout the ebb tide, with plume length varying between 3.5 km and 7 km. During the beginning and end of ebb tide, the plume stays closer to the coast, reaching a maximum width of ~2 km, where the currents are weaker. During the middle phase of the ebb tide, when currents are stronger, the plume drifts slightly away from the coast and covers a larger area. In both cases, the plume area does not extend beyond the underwater banks, which can be noticed on the bathymetry maps as two shallow water regions 5 km off the coast (Figure 5a).

During the flood tide, the tidal stream offshore runs southwards which is very well indicated by the plume direction (Figure 5c). Again, this type of flow is consistent throughout the flood tide. The plume flows closer to the coast than during the ebb tide.

4. Discussion

The probability density maps of the plume distribution presented above are based on clear-sky thermal imagery from ASTER and TIRS with low cloud cover. For Heysham, we obtained 46 scenes (40 daytime and six night-time images), of which 23 depict the ROI during the ebb tide and 23 during the flood tide. For Sizewell we obtained 48 scenes (47 daytime and one night-time image), with 16 under ebb tide and 32 under flood tide conditions. Over the operational time of both instruments, the acquired number of images is not sufficient to monitor the thermal plume on a daily basis. It is, however, appropriate to use those images for detailed characterisation in the context of tidal effects on plume dispersion.

Detecting the plume based on thermal thresholds proves useful in understanding the plume behaviour associated with the tidal regimes. When the plume is extending towards the open water and warm water, puddles are localised very close to the exposed sand bank areas or land and are not extensive, and it is easier to delineate the plume from the rest of the waters. However, under certain circumstances, it can be more complicated to delineate the plume properly and use the imagery for further analysis. When the thermal plume is trapped close to the coastline, during summer periods where the bathymetry is shallow, the plume and the warmer shallow coastal waters can have similar SST values. In those situations it is challenging to distinguish the plume from those warm shallow waters very close to the land. This issue has been addressed through land mask expansion, automatically excluding a narrow belt of warm coastal waters. This expansion does not cause the plume to be mistakenly missed, as in all images, the detected plume has width greater than the added mask expansion and continues to disperse offshore. However, it is possible that for other shallow water locations with a plume limited in area or trapped close to the coast, such mask expansion could exclude a part of the detected plume.

This technique of plume detection can be applied to data from other sensors while adapting the temperature threshold accordingly. Langford (1990) proposed as a definition of a thermal plume that the water that is warmer by 0.5 K than the temperature of the ambient waters [40]. This threshold, however, will not always be appropriate and one should include the uncertainty associated with the chosen sensors and retrieval method. In case of using other sensors, the sensor should have at least one TIR channel for temperature retrieval. A combination of Green and near-IR or Green and SWIR channels would also be useful in order to apply the water detection algorithm prior to the plume detection; otherwise, a combination of techniques would have to be applied to exclude land and cloud pixels.

We consider our findings in comparison with other studies, which include field campaigns and modelling. The findings on plume direction and location in the Heysham area are consistent with a field campaign carried out by EDF Energy (EDF Energy, classified report) during one flood and one ebb tide. The direction of the detected plume captured by the satellite imagery is in agreement with the boat survey for both types of tide. The detected plume spatial extent observed during the flood tide is greater in the direction of the shore from the satellite imagery than the boat survey. This is because

the coastal waters near the shore were too shallow for the research vessel, which restricted access and therefore limited the investigated area.

The findings on flow switching in the Sizewell area are consistent with a study that used modelling techniques [37,41]. A study carried out by the British Energy Estuarine and Marine Studies (BEEMS) programme [41] used a 3D hydrodynamic model to investigate the plume direction and surface area. They looked at four infrared images of plumes near Sizewell taken on the same day during different tide phases in order to validate their model outputs. The probability density maps for flood and ebb tide based on multiple satellite images are in agreement with the BEEMS modelling study and the infrared images of one sample day, which were included in the BEEMS report. Both the direction and the extent of the plume is consistent between BEEMS and this study.

In this paper, we are interested in observations of the plume itself. However, combining our satellite observations with a hydrodynamic model would be a good tool to describe coastal tidal dynamics [42]. The observations could be used to validate the simulations, as well as combined with the model to develop a three dimensional simulation of the plume. Modelling would enable investigation of subsurface processes that influence plume dispersion. Having a full understanding of the plume dynamics through a hydrodynamic model is important for recognising potential ecological impacts [43]. This, in turn, will enable better information to be developed for facilities, such as industrial power stations, local communities, leisure facilities and the centres for biodiversity of marine species.

5. Conclusions

Satellite imagery provides valuable additional information that contributes to better understanding of the impact of tides on plume dispersion. The number of clear-sky images (on average nine scenes per year depending on location) is too low for day-to-day monitoring of a thermal plume, but it is adequate for detailed characterisation in the context of tidal effects on detected plumes. Industrial plumes are released from a point source and due to higher-than-ambient temperature reveal the direction of the surface water currents. Conditional probability maps of detected plumes are produced using multiple observations from different platforms, expanding the data from 2000 to 2019 sample with daytime and night-time imagery across different seasons and years. The direction and the size of detected thermal plumes depend on: the phase of the tide and the strength of the surface currents. For Heysham, as an example of intertidal embayment, the detected plume resembled a narrow, elongated region of 5–7 km in length flowing south-westward during the ebb tide and a restricted pool of warmer-than ambient water reaching 3.5–4 km offshore during flood tide. For Sizewell, as an example of open water exposure, the detected plume was an elongated area of water ranging from 3.5 to 10 km in length in the same direction as the tidal currents (southward for the flood tide and northward for the ebb tide). Such analysis, compared to traditional methods that use field campaigns, can cost-effectively inform the power stations of the surface plume behaviour during certain conditions and indicate the area of thermal contrast. With much satellite data from various sensors freely available through online platforms, such observations might prove useful compared to expensive one day campaigns. Understanding the dispersion of the plume is also essential to aid understanding of any potential ecological impacts.

Author Contributions: The lead author, A.F., undertook the majority of this work with supervision from C.E.B. and C.J.M.

Funding: The first author was sponsored by EDF Energy PhD Studentship.

Acknowledgments: We would like to thank the Institute of Environmental Analytics at the University of Reading for developing an interface for downloading the data. We used Landsat 8 and ASTER data available from the U.S. Geological Survey (freely available on the U.S. Geological Survey Earth Explorer website). For the tidal analysis we have used Environment Agency tide gauge data from the real-time data API (Beta). This work has used sea current data from the Norwegian Meteorological Institute, land elevation from ASTER GDEM and bathymetry from EmodNET of EDF Energy R&G Natural Hazard Team for their support.

Conflicts of Interest: The authors declare no conflicts of interest.

Abbreviations

The following abbreviations are used in this manuscript.

ASTER	Advanced Spaceborne Thermal Emission and Reflection Radiometer
BEEMS	British Energy Estuarine and Marine Studies
BT	brightness temperature
CCI	Climate Change Initiative
ECMWF	European Centre for Medium-Range Weather Forecasts
EMODnet	European Marine Observation and Data Network
ESA	European Space Agency
GDEM	Global Digital Elevation model
MET Norway	Norwegian Meteorological Institute
METI	Ministry of Economy, Trade and Industry in Japan
MNDWI	Modified Normalised Water Difference Index
NASA	National Aeronautics and Space Administration
NDWI	Normalised Difference Water Index
near-IR	near infrared
netCDF	Network Common Data Format
NTNG	National Tide Gauge Network
NWP	Numerical Weather Prediction
OE	Optimal Estimation
OLI	Operational Land Imager
RGB	red green blue
ROI	region of interest
RTM	Radiative Transfer Model
RTTOV	Radiative Transfer for TOVS (model)
SST	sea surface temperature
SWIR	short-wave infrared
TIR	thermal infrared
TIRS	Thermal Infrared Sensor
USGS	United States Geological Survey
VNIR	visible and near infrared

References

1. Islam, M.A.; Mitra, D.; Dewan, A.; Akhter, S.H. Coastal multi-hazard vulnerability assessment along the Ganges deltaic coast of Bangladesh—A geospatial approach. *Ocean. Coast. Manag.* **2016**, *127*, 1–15.
2. Peponi, A.; Morgado, P.; Trindade, J. Combining Artificial Neural Networks and GIS Fundamentals for Coastal Erosion Prediction Modeling. *Sustainability* **2019**, *11*, 975.
3. Harik, G.; Alameddine, I.; Maroun, R.; Rachid, G.; Bruschi, D.; Garcia, D.A.; El-Fadel, M. Implications of adopting a biodiversity-based vulnerability index versus a shoreline environmental sensitivity index on management and policy planning along coastal areas. *J. Environ. Manag.* **2017**, *187*, 187–200. [CrossRef] [PubMed]
4. Mei, C.C.; Liu, P. Surface waves and coastal dynamics. *Annu. Rev. Fluid Mech.* **1993**, *25*, 215–240. [CrossRef]
5. Klevanny, K.; Matveyev, G.; Voltzinger, N. An integrated modelling system for coastal area dynamics. *Int. J. Numer. Methods Fluids* **1994**, *19*, 181–206. [CrossRef]
6. De Vriend, H.J. Mathematical modelling and large-scale coastal behaviour: Part 1: physical processes. *J. Hydraul. Res.* **1991**, *29*, 727–740. [CrossRef]
7. Dalrymple, R.A.; Rogers, B. Numerical modeling of water waves with the SPH method. *Coast. Eng.* **2006**, *53*, 141–147.
8. Durán-Colmenares, A.; Barrios-Piña, H.; Ramírez-León, H. Numerical modeling of water thermal plumes emitted by thermal power plants. *Water* **2016**, *8*, 482. [CrossRef]

9. Alesheikh, A.A.; Ghorbanali, A.; Nouri, N. Coastline change detection using remote sensing. *Int. J. Environ. Sci. Technol.* **2007**, *4*, 61–66. [CrossRef]
10. Paduan, J.D.; Rosenfeld, L.K. Remotely sensed surface currents in Monterey Bay from shore-based HF radar (Coastal Ocean Dynamics Application Radar). *J. Geophys. Res. Ocean.* **1996**, *101*, 20669–20686. [CrossRef]
11. Dabuleviciene, T.; Kozlov, I.; Vaiciute, D.; Dailidiene, I. Remote Sensing of Coastal Upwelling in the South-Eastern Baltic Sea: Statistical Properties and Implications for the Coastal Environment. *Remote Sens.* **2018**, *10*, 1752. [CrossRef]
12. Abascal Zorrilla, N.; Vantrepotte, V.; Gensac, E.; Huybrechts, N.; Gardel, A. The Advantages of Landsat 8-OLI-Derived Suspended Particulate Matter Maps for Monitoring the Subtidal Extension of Amazonian Coastal Mud Banks (French Guiana). *Remote Sens.* **2018**, *10*, 1733. [CrossRef]
13. Huang, S.J.; Lin, J.T.; Lo, Y.T.; Kuo, N.J.; Ho, C.R. The Coastal Sea Surface Temperature Changes Near the Nuclear Power Plants of Northern Taiwan Observed from Satellite Images. In Proceedings of the OCEANS 2014-TAIPEI, Taipei, Taiwan, 7–10 April 2014; pp. 1–5.
14. Muthulakshmi, A.; Natesan, U.; Ferrer, V.A.; Deepthi, K.; Venugopalan, V.; Narasimhan, S. A novel technique to monitor thermal discharges using thermal infrared imaging. *Environ. Sci. Process. Impacts* **2013**, *15*, 1729–1734. [CrossRef] [PubMed]
15. Dai, X.; Guo, Z.; Chen, Y.; Ma, P.; Chen, C. Monitoring of Thermal Plume Discharged from Thermal and Nuclear Power Plants in Eastern China Using Satellite Images. In Proceedings of the 2016 IEEE International Geoscience and Remote Sensing Symposium (IGARSS), Beijing, China, 10–15 July 2016; pp. 7659–7662.
16. Ma, P.; Dai, X.; Guo, Z.; Wei, C.; Ma, W. Detection of thermal pollution from power plants on China's eastern coast using remote sensing data. *Stoch. Environ. Res. Risk Assess.* **2017**, *31*, 1957–1975. [CrossRef]
17. Tang, D.; Kester, D.R.; Wang, Z.; Lian, J.; Kawamura, H. AVHRR satellite remote sensing and shipboard measurements of the thermal plume from the Daya Bay, nuclear power station, China. *Remote Sens. Environ.* **2003**, *84*, 506–515.
18. Ahn, Y.H.; Shanmugam, P.; Lee, J.H.; Kang, Y.Q. Application of satellite infrared data for mapping of thermal plume contamination in coastal ecosystem of Korea. *Mar. Environ. Res.* **2006**, *61*, 186–201. [CrossRef]
19. Xu, J.; Zhu, L.; Jiang, J.; Li, J.; Zhao, S.; Yuan, L. Monitoring thermal discharge in Daya Bay plant based on thermal infrared band of HJ-1B and TM remote sensing data. *China Environ. Sci.* **2014**, *34*, 1181–1186.
20. Anupkumar, B.; Rao, T.; Venugopalan, V.; Narasimhan, S. Thermal mapping in the Kalpakkam Coast (Bay of Bengal) in the vicinity of Madras atomic power station. *Int. J. Environ. Stud.* **2005**, *62*, 473–485. [CrossRef]
21. Zoran, M. Nuclear Power Plant's Water Thermal Plume Assessment by Satellite Remote Sensing Data. In Proceedings of the Global Conference on Global Warming, Lisbon, Portugal, 11–14 July 2011; pp. 11–14.
22. Xu, H. Modification of normalised difference water index (NDWI) to enhance open water features in remotely sensed imagery. *Int. J. Remote Sens.* **2006**, *27*, 3025–3033. [CrossRef]
23. McFeeters, S.K. The use of the Normalized Difference Water Index (NDWI) in the delineation of open water features. *Int. J. Remote Sens.* **1996**, *17*, 1425–1432. [CrossRef]
24. Kelly, J.T.; Gontz, A.M. Using GPS-surveyed intertidal zones to determine the validity of shorelines automatically mapped by Landsat water indices. *Int. J. Appl. Earth Obs. Geoinf.* **2018**, *65*, 92–104. [CrossRef]
25. Pardo-Pascual, J.; Sánchez-García, E.; Almonacid-Caballer, J.; Palomar-Vázquez, J.; Priego De Los Santos, E.; Fernández-Sarría, A.; Balaguer-Beser, Á. Assessing the accuracy of automatically extracted shorelines on microtidal beaches from Landsat 7, Landsat 8 and Sentinel-2 Imagery. *Remote Sens.* **2018**, *10*, 326. [CrossRef]
26. Merchant, C.; Le Borgne, P.; Marsouin, A.; Roquet, H. Optimal estimation of sea surface temperature from split-window observations. *Remote Sens. Environ.* **2008**, *112*, 2469–2484. [CrossRef]
27. Merchant, C.J.; Embury, O.; Bulgin, C.E.; Block, T.; Corlett, G.; Good, S.A.; Mittaz, J.; Rayner, N.A.; Berry, D.; Eastwood, S.; et al. Satellite-based time-series of sea surface temperature since 1981 for climate applications. *Nat. Sci. Data* **2019**, In press.
28. Saunders, R. Coauthors, 2013: RTTOV-11 Science and Validation Report. Available online: https://www.nwpsaf.eu/site/download/documentation/rtm/docs_rttov11/rttov11_svr.pdf (accessed on 29 July 2019).
29. Hocking, J.; Rayer, P.; Rundle, D.; Saunders, R.; Matricardi, M.; Geer, A.; Brunel, P.; Vidot, J. *RTTOV v11 Users Guide, NWP-SAF Report, Met*; Office: Exeter, UK, 2014.
30. Dee, D.P.; Uppala, S.; Simmons, A.; Berrisford, P.; Poli, P.; Kobayashi, S.; Andrae, U.; Balmaseda, M.; Balsamo, G.; Bauer, d.P.; et al. The ERA-Interim reanalysis: Configuration and performance of the data assimilation system. *Q. J. R. Meteorol. Soc.* **2011**, *137*, 553–597. [CrossRef]

31. Merchant, C.J.; Embury, O.; Roberts-Jones, J.; Fiedler, E.; Bulgin, C.E.; Corlett, G.K.; Good, S.; McLaren, A.; Rayner, N.; Morak-Bozzo, S.; et al. Sea surface temperature datasets for climate applications from Phase 1 of the European Space Agency Climate Change Initiative (SST CCI). *Geosci. Data J.* **2014**, *1*, 179–191. [CrossRef]
32. Gonzalez, R.C.; Woods, R.E. *Digital Image Processing*; Addison-Wesley: Reading, MA, USA, 1992; Volume 2.
33. Barsi, J.A.; Markham, B.L.; Montanaro, M.; Gerace, A.; Hook, S.J.; Schott, J.R.; Raqueno, N.G.; Morfitt, R. Landsat-8 TIRS Thermal Radiometric Calibration Status. In Proceedings of the Earth Observing Systems XXII. International Society for Optics and Photonics, San Diego, CA, USA, 6–10 August 2017; Volume 10402, p. 104021G.
34. Abrams, M.; Hook, S.; Ramachandran, B. *ASTER User Handbook*; Jet Propulsion Laboratory: Pasadena, CA, USA, 2002; pp. 45–54.
35. Mason, D.; Scott, T.; Dance, S. Remote sensing of intertidal morphological change in Morecambe Bay, UK, between 1991 and 2007. *Estuar. Coast. Shelf Sci.* **2010**, *87*, 487–496. [CrossRef]
36. Coomber, D.P.M.; Hanson, J.D. *Estuaries Management Plans: Coastal Processes and Conservation, Morecambe Bay*; University of Glasgow: Glasgow, UK, 1994; p. 79.
37. Lees, B.J. Observations of tidal and residual currents in the Sizewell–Dunwich area, East Anglia, UK. *Dtsch. Hydrogr. Z.* **1983**, *36*, 1–24. [CrossRef]
38. Pye, K.; Blott, S.J. Coastal processes and morphological change in the Dunwich-Sizewell area, Suffolk, UK. *J. Coast. Res.* **2006**, *22*, 453–473. [CrossRef]
39. Sinha, B.; Pingree, R. The principal lunar semidiurnal tide and its harmonics: baseline solutions for M2 and M4 constituents on the North-West European Continental Shelf. *Cont. Shelf Res.* **1997**, *17*, 1321–1365. [CrossRef]
40. Langford, T. *Ecological Effects of Thermal Discharges*; Springer Science & Business Media: Boston, MA, USA, 1990.
41. Estuarine, B.E.; Panel, M.S.E. *Thermal Standards for Cooling Water from New Build Nuclear Power Stations*; British Energy Estuarine & Marine Studies: Severn Estuary, UK, 2011. Available online: https://infrastructure.planninginspectorate.gov.uk/wp-content/ipc/uploads/projects/\EN010001/EN010001-005198-HPC-NNBPEA-XX-000-RET-000212%201.pdf (accessed on 29 July 2019).
42. Davies, A.; Sauvel, J.; Evans, J. Computing near coastal tidal dynamics from observations and a numerical model. *Cont. Shelf Res.* **1985**, *4*, 341–366. [CrossRef]
43. Carniello, L.; Silvestri, S.; Marani, M.; D'Alpaos, A.; Volpe, V.; Defina, A. Sediment dynamics in shallow tidal basins: In situ observations, satellite retrievals, and numerical modeling in the Venice Lagoon. *J. Geophys. Res. Earth Surf.* **2014**, *119*, 802–815. [CrossRef]